

Hexagonal convection patterns in atomistically simulated fluids

D. C. Rapaport*

Physics Department, Bar-Ilan University, Ramat-Gan 52900, Israel

(Dated: August 07, 2005)

Molecular dynamics simulation has been used to model pattern formation in three-dimensional Rayleigh–Bénard convection at the discrete-particle level. Two examples are considered, one in which an almost perfect array of hexagonally-shaped convection rolls appears, the other a much narrower system that forms a set of linear rolls; both pattern types are familiar from experiment. The nature of the flow within the convection cells and quantitative aspects of the development of the hexagonal planform based on automated polygon subdivision are analyzed. Despite the microscopic scale of the system, relatively large simulations with several million particles and integration timesteps are involved.

PACS numbers: 47.54.-r, 02.70.Ns, 47.27.T-

The spontaneous emergence of flow patterns in externally driven fluids is one of the more fascinating aspects of fluid dynamics, and a great deal of experimental and theoretical effort has been spent studying such phenomena over the past century. Theoretical fluid dynamics has successfully ignored the underlying atomicity, describing the dynamics in terms of nonlinear partial differential equations for continuous fields; analysis of flow instability within this framework demands approximations whose consequences are not always readily assessed. Ideally, one would like to understand flow instability in terms of the behavior at the microscopic level by looking beyond the continuum representation to address the dynamics of the molecules themselves, albeit at considerable computational cost; given sufficiently many molecules followed for an adequate time interval, one can reasonably expect to see the same kind of behavior (initially in a qualitatively correct form, then, with even larger systems, also quantitatively). The ability to simultaneously encompass the dynamics both at the molecular level and the scale at which the cooperativity underlying structured flow becomes manifest is an important step in trying to break free of the limitations of traditional continuum fluid dynamics.

Accomplishing this goal calls for molecular dynamics (MD) simulation, a technique in broad general use, but less so for fluid dynamics (quite likely due to Avogadro’s tyranny – an apparent need for extremely large systems to accommodate the phenomena). A very early MD effort related to bridging the gap between atomistic dynamics and fluid behavior at the continuum level was understanding long-time effects due to correlations in atomic trajectories [1], but it was only much later that actual MD simulation of complex flow was attempted. Initial efforts were confined to two dimensions, starting with the wakes of obstructed flows [2, 3] and followed by Rayleigh–Bénard (RB) convection [4, 5, 6, 7, 8, 9]; the study of Taylor–Couette flow [10, 11] demonstrated that complex

three-dimensional flow could also be dealt with and, subsequently, the Rayleigh–Taylor instability was also modeled [12]. Other instances of MD contributing to fluid dynamics include the moving interface between immiscible liquids undergoing Poiseuille flow [13] and droplet breakup in liquid jets [14]. The present study describes the application of the MD approach to the full three-dimensional RB problem, where the behavior is potentially far richer than in two dimensions, and where simulation is more closely related to experiment; the ability to tackle increasingly demanding MD simulations, both in terms of size and duration, reflects the availability of increasingly powerful and affordable computing resources.

The RB phenomenon – the rich variety of flow patterns produced by convection in a fluid layer heated from below – continues to be a problem of great interest [15, 16, 17, 18, 19]. The principal dimensionless quantity governing the behavior is the Rayleigh number, $Ra = \alpha g L_z^3 \Delta T / \nu \kappa$, where α , ν and κ are the thermal expansion coefficient, kinematic viscosity and thermal diffusivity, L_z is the layer height, g the gravitational acceleration, and $\Delta T = T_1 - T_0$ is the temperature difference between the lower hot wall T_1 and the upper cold wall T_0 ; a critical value Ra_c marks the onset of convection, where buoyancy overcomes viscous drag, and convection replaces conduction as the preferred thermal transport mechanism.

Theory is simplified by the Boussinesq approximation, in which it is assumed the only temperature-dependent fluid property is the density. Ra_c can be computed for various kinds of boundary conditions [15], as can the wavelength λ of the convection pattern at criticality, but not the actual planform (e.g., rolls, spirals and hexagons). Roll width (typically $\approx L_z$) represents a compromise; wide rolls reduce both viscous drag and diffusive heat transfer between ascending hot and descending cold streams, whereas narrow rolls reduce shear losses close to nonslip walls. Hexagonal patterns were once associated with non-Boussinesq fluids [18, 20] (and are better known in convection driven by surface tension); the flow direction at the cell center is determined by the temperature dependence of ν and differs for gases and liquids.

*Electronic address: rapaport@mail.biu.ac.il

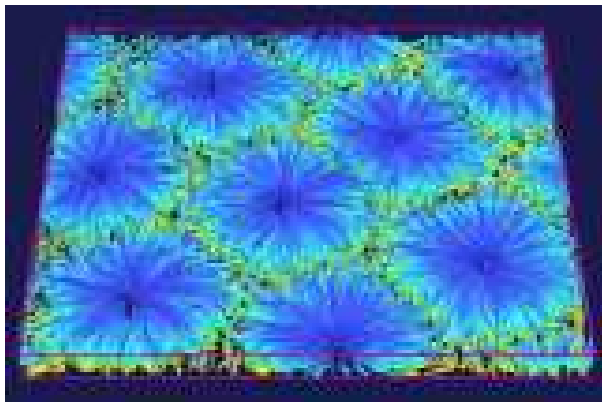


FIG. 1: (Color online) Final streamline plot for the large rectangular system #A showing the hexagonal cell pattern; the streamlines are color coded to indicate temperature variation (ranging from red for hot to blue for cold).

Hexagons are now known to occur in (essentially) Boussinesq systems above Ra_c [21, 22], even forming coexisting regions with opposite flows at the cell centers, a phenomenon not attributable to variable ν .

The MD simulation [23] considers a fluid of soft-sphere atoms with a short-ranged, repulsive interaction $u(r) = 4\epsilon[(\sigma/r)^{12} - (\sigma/r)^6]$, with a cutoff at $r_c = 2^{1/6}\sigma$. In the dimensionless MD units used subsequently, σ and ϵ determine length and energy, while temperature is defined by setting $k_B = 1$; in the case of Argon, $\sigma = 3.4\text{\AA}$, $\epsilon/k_B = 120\text{ K}$, and the unit of time is 2.16 ps. The top and bottom thermal walls of the system are each formed from a layer of fixed atoms arranged as a lattice, spaced to ensure roughness and impenetrability; lateral boundaries are periodic. The temperature gradient is produced by rescaling the velocities of those atoms adjacent (within a range of 1.3) to the thermal walls; rescaling occurs every 20 timesteps to allow the effect to propagate without unduly affecting the dynamics, and is applied to atoms moving away from the walls. In the initial state, atoms are placed on the sites of a regular grid, with random velocities corresponding to a uniform vertical temperature gradient. The integration timestep is 0.004. In view of the extensive computations required, parallel processing based on spatial decomposition is used.

Flow analysis entails spatial coarse-graining, in which a grid subdivision is applied to the region and the mean properties (velocity, temperature, density) for each grid cell are evaluated for its occupant atoms. This is repeated every 20 timesteps and averages over 100 successive measurements recorded, with typical grid sizes of 5–6 horizontally and 3 vertically (≈ 30 atoms per grid cell); this represents a compromise between capturing the fine spatial and temporal detail of the developing convection patterns and reducing noise due to thermal fluctuations.

Two of a series of runs are described in detail below; the eventual outcomes of both are organized convection cell patterns, a hexagonal array in the case of system

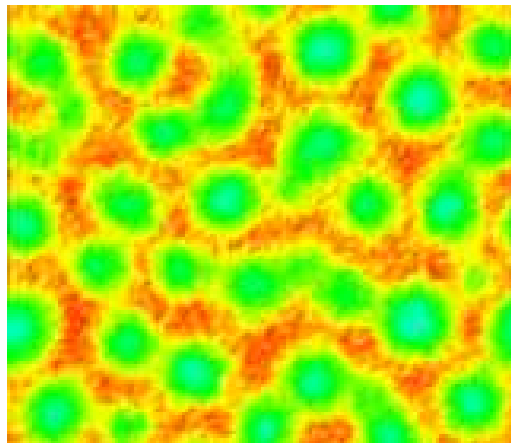


FIG. 2: (Color online) Early temperature distribution near the lower wall.

#A and a set of linear rolls for #B. System #A contains $N_a = 3\,507\,170$ atoms (of which $N_w = 447\,458$ are fixed in the walls) and is run for a total of 3.19×10^6 timesteps ($= 2.8 \times 10^{-8}\text{ s}$). The region size is $L_x \times L_y \times L_z = 521 \times 451 \times 35.3$; despite the smallness of L_z (a mere 120\AA), the layer thickness exceeds the value 25 used in the Taylor–Couette study [10, 11]. Since the rate of pattern change slows as features become larger, a reflection of the underlying horizontal diffusion processes, the long run is needed to ensure a final steady state is reached. The smaller system #B has $L_y = 65$ (L_x and L_z are unchanged), resulting in a more modest $N_a = 506\,696$ (with $N_w = 64\,328$), and a run length of 0.48×10^6 timesteps. In both cases, $T_0 = 1$, $T_1 = 10$; the value $g = 3\Delta T/2L_z$ ensures equality of the potential and kinetic energy changes across the layer and avoids excessive density variation. Large gradients and fields are the norm for MD flow studies that must deal with relatively small regions, here compensating for the small L_z to ensure an adequate value of Ra ; $\Delta T/T_0$ is large compared with experiment (where $\Delta T/T_0 \approx 0.01$ or less), and $g = 2.7 \times 10^{12} g_{earth}$ (the variation in gravitational potential across the layer, gL_z , is only 8 times that of [12]). The total computation time for system #A amounts to approximately 6 cpu-months on a 2 GHz Intel Pentium processor, with the actual run using an 8-cpu cluster.

The final state of system #A is shown in Fig. 1 as a streamline plot that reveals the full three-dimensional flow structure; the curved tracks (color coded to show temperature variation) are derived from the coarse-grained grid (size $96 \times 82 \times 12$). The most prominent feature is the array of hexagonal convection cells extending across the full depth of the layer, with cold fluid descending at the cell centers. The cell array is free to orient itself to accommodate a preferred λ for the particular size and shape of the periodic container; animated three-dimensional visualization allows following the pattern development as cells grow and merge (not shown).

Figure 2 shows the horizontal temperature distribu-

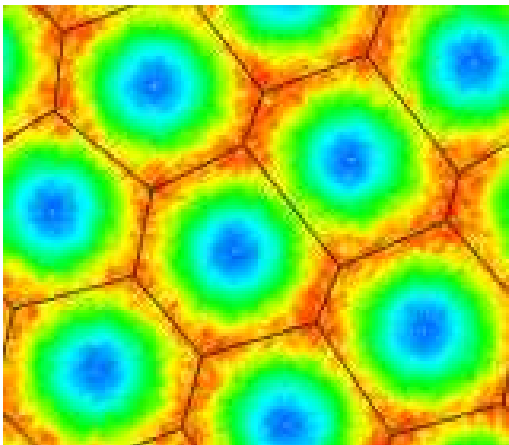


FIG. 3: (Color online) Final temperature distribution with Voronoi polygon subdivision superimposed.

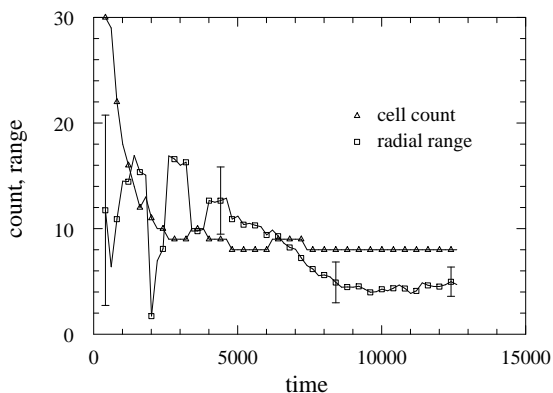


FIG. 4: Graphs showing time-dependence (dimensionless MD units) of the cell count and the mean radial range (typical fluctuations are included for the latter).

tion at a distance $\approx L_z/5$ from the hot wall early in the run, after the onset of convection but before a regular cell pattern develops. The distribution at the end of the run appears in Fig. 3, with the periodic cell array clearly visible. Superimposed on this image is a polygon subdivision produced by an automated Voronoi analysis of a slice through the flow structure (limited system size cannot accommodate the large aspect ratios $L_x/L_z > 100$ used experimentally, as opposed to 15 here, that yield extended patterns amenable to Fourier and other forms of analysis [24]); cell centers marked by white spots are located at each of the local temperature minima (or at the downward flow maxima) and the plane subdivided into polygons in which the region nearer to a particular center than to any other is assigned to its polygon. The resulting polygon set provides a good fit to the cell boundaries where hot upward flow is strongest (the fit quality improves as the run progresses), and is used in the quantitative analysis below.

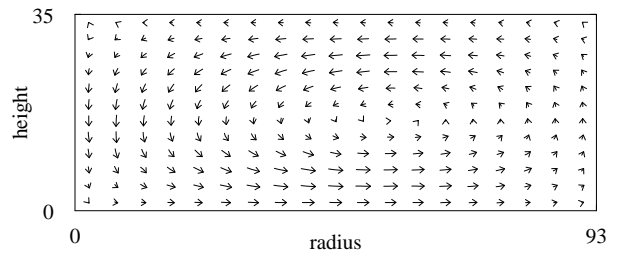


FIG. 5: Flow field azimuthally averaged over all cells; the axes measure the radial distance from the cell center and the height above the hot wall (dimensionless MD units).

The time-dependence of two prominent features of the polygon arrays is shown in Fig. 4. The polygon count falls from an initial value of ≈ 30 to the eventual 8 at time $t \approx 5000$, it then increases to 9 and finally drops back to 8 at $t \approx 8000$ as cells split and merge; this behavior is an indication of the slow relaxation processes that the simulations must be able to cover. The mean deviation of the polygon shape from regularity, expressed as the range of radial distances of the nearest and furthest vertices of each polygon, shows a more gradual convergence to the final value of 4.5, which is just 5% of the mean radius. Other planform properties include the mean distance from the center to the nearest point on an edge, $\lambda_{hex}/2$, whose final value is 93 ± 1 , the mean polygon area that is inversely proportional to the count, and the area variation that falls to a minimum of $\pm 2\%$ of the mean in the final state. The average number of vertices per polygon must be 6; the spread of values falls to zero as the final state is neared. These results quantify what is observed directly, namely an initially disordered set of small convection cells that grow, merge and rearrange, culminating in what appears to be a stable array of hexagonal cells; the final wavelength $\lambda_{hex} = 5.27 L_z$, a value not much larger than the experimental $4 L_z$ [21] (a lower λ_{hex} is reported in [22]); the characteristic size of the cells present in the early, irregular pattern is about half this value (Fig. 2).

Details of the flow profile inside a single convection cell appear in Fig. 5. The arrow plot shows the radial and vertical components of the flow field within the cells, averaged over all cells of the final state, and is evaluated by projecting the flow velocity onto a series of vertical planes arranged as radial spokes around each cell center, with only grid cells that intersect the planes contributing. The maximum arrow length corresponds to a speed of 0.52. While average descending flow appears faster than ascending, this is consistent with the toroidal roll shape that allows more space for the latter. The nonslip nature of the flow at the lower wall is partly masked by coarse-graining, but flow rate is seen to decrease near the wall (the effectiveness of the nonslip mechanism is better appreciated in small systems run interactively). Local temperature (not shown) increases radially outwards from the cell core and drops with height; its estimation

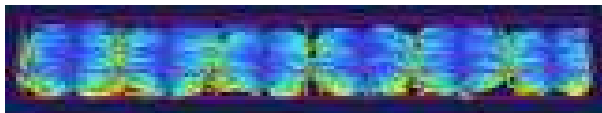


FIG. 6: (Color online) Final streamline plot for system #B showing the linear roll pattern.

is problematic because the contribution of nonuniform bulk flow cannot be fully removed, and thermalization includes atoms interacting with the walls, so the measured range is 0.84–11.4 (rather than 1–10), but the gradual variation across the roll profile and the absence of high gradients near the walls (except where the cool downflow initially encounters the hot wall) are evidence of efficient heat exchange between fluid and walls. Local density varies from 0.58 at the cell core to 0.38 at the periphery (the overall mean is 0.4).

The final state of run #B consists of a set of 6 pairs of counter-rotating rolls. Fig. 6 shows the streamline plot; the wavelength λ_{roll} ($2 \times$ roll diameter) = $87 = 2.46 L_z$ (note that 7 roll pairs would have produced a value close to the theoretical $\lambda_{roll} = 2.016 L_z$ [15]). The wavelength ratio from runs #A and #B is $\lambda_{hex}/\lambda_{roll} = 2.14$; the experimental ratio for coexisting hexagons and rolls is 1.2–1.3 [21]. At an early stage in run #B there is an unsuccessful attempt to form a pair of longitudinal rolls.

When T_1 is lowered to 6 the roll pattern in system #B is unchanged, but at $T_1 = 4$ the results are noisy and roll structure is not readily discerned, though it is still present in weakened form. Strong finite-size effects due to small L_z erase any hint of a sharp transition between conducting and convecting states. The fluid has its own intrinsic thermodynamic and transport properties determined by

the soft-sphere model and, since $\Delta T/T_0$ is large, does not satisfy the Boussinesq condition; estimating Ra based on Enskog theory and a simple equation of state [7, 8] is inappropriate here due to the variation of ν and κ across the layer.

These simulations (and work in progress) provide strong confirmation that MD is capable of reproducing known fluid dynamical behavior; the unique aspect of this approach is that, while following the dynamics at the atomic scale where the underlying causes of flow instability and self-organization are to be found, it simultaneously embraces the continuum scale where fluid behavior is manifest and scant evidence of atomism remains. Increasing computer performance (parallel computers are ideal for simulations of this kind) allows ever-larger systems to be modeled, although this growth is tempered by the fact that computation time increases not only in proportion to system size but also due to slow diffusive processes that govern structure development. Larger systems reduce the necessarily high thermal and velocity gradients and help eliminate spurious finite-size effects, allowing closer correspondence with experiment. The outcome of the present MD study has obvious implications for future MD exploration of fluid dynamical phenomena.

Acknowledgments

This work was begun during a visit to the University of Edinburgh in the last millennium that was supported by the TRACS program at EPCC; S. Pawley is thanked for his kind hospitality.

-
- [1] B. J. Alder and T. E. Wainwright, Phys. Rev. A **1**, 18 (1970).
 - [2] D. C. Rapaport and E. Clementi, Phys. Rev. Lett. **57**, 695 (1986).
 - [3] D. C. Rapaport, Phys. Rev. A **36**, 3288 (1987).
 - [4] M. Mareschal and E. Kestemont, J. Stat. Phys. **48**, 1187 (1987).
 - [5] D. C. Rapaport, Phys. Rev. Lett. **60**, 2480 (1988).
 - [6] M. Mareschal, M. M. Mansour, A. Puhl, and E. Kestemont, Phys. Rev. Lett. **61**, 2550 (1988).
 - [7] A. Puhl, M. M. Mansour, and M. Mareschal, Phys. Rev. A **40**, 1999 (1989).
 - [8] D. C. Rapaport, Phys. Rev. A **46**, 1971 (1992).
 - [9] D. C. Rapaport, Phys. Rev. A **46**, R6150 (1992).
 - [10] D. Hirshfeld and D. C. Rapaport, Phys. Rev. Lett. **80**, 5337 (1998).
 - [11] D. Hirshfeld and D. C. Rapaport, Phys. Rev. E **61**, R21 (2000).
 - [12] K. Kadau, T. C. Germann, N. G. Hadjiconstantinou, P. S. Lomdahl, G. Dimonte, B. L. Holian, and B. J. Alder, PNAS **101**, 5851 (2004).
 - [13] J. Koplik, J. R. Banavar, and J. Willemsen, Phys. Fluids A **1**, 781 (1989).
 - [14] M. Moseler and U. Landman, Science **289**, 1165 (2000).
 - [15] S. Chandrasekhar, *Hydrodynamic and Hydromagnetic Stability* (Oxford University Press, Oxford, 1961).
 - [16] C. Normand, Y. Pomeau, and M. G. Velarde, Rev. Mod. Phys. **49**, 581 (1977).
 - [17] P. Bergé and M. Dubois, Contemp. Phys. **25**, 535 (1984).
 - [18] E. L. Koschmieder, *Bénard Cells and Taylor Vortices* (Cambridge University Press, Cambridge, 1993).
 - [19] E. Bodenschatz, W. Pesch, and G. Ahlers., Annu. Rev. Fluid Mech. **32**, 709 (2000).
 - [20] E. Bodenschatz, J. R. de Bruyn, G. Ahlers, and D. S. Cannell, Phys. Rev. Lett. **67**, 3078 (1991).
 - [21] M. Assenheimer and V. Steinberg, Phys. Rev. Lett. **76**, 756 (1996).
 - [22] K. M. S. Bajaj, D. S. Cannell, and G. Ahlers, Phys. Rev. E **55**, R4869 (1997).
 - [23] D. C. Rapaport, *The Art of Molecular Dynamics Simulation* (Cambridge University Press, Cambridge, 2004), 2nd ed.
 - [24] D. A. Egolf, I. V. Melnikov, and E. Bodenschatz, Phys. Rev. Lett. **80**, 3228 (1998).